Photoelectrocatalysis on TiO_2 Derived from Titanium Acetylacetonate: Effect of Decomposition Temperature

Anna Ulyankina [1], Daria Bondareva[1], Tatiana Belichenko[1], Yash Kataria[1]*, Aydar Rakhmatullin[2], Igor Leontyev[3], Nina Smirnova[1]

[1] *Research Institute "Nanotechnologies and New Materials", Platov South-Russian State Polytechnic University (NPI), Novocherkassk 346428, Russia*

[2] *Conditions Extrêmes et Matériaux: Haute Température et Irradiation, CEMHTI, UPR 3079–CNRS Univ. Orléans, 45071 Orléans, France*

[3] *Department of Physics, Southern Federal University, Rostov-on-Don, Russia*

* *Corresponding Author. E-mail: katariayash1603@gmail.com (Yash Kataria)*

Abstract

Photoelectrocatalytic (PEC) water splitting utilizing titanium dioxide (TiO_2) photoanodes presents a promising avenue for sustainable hydrogen production. Understanding the correlation linking the synthesis conditions to structural and phase evolution of semiconductor materials, which is essential for the development of photoanodes with improved PEC activity, remains challenging. This study aims to elucidate the structure- and phase-dependent PEC activity of TiO_2 nanoparticles (NPs) obtained via the non-isothermal decomposition of titanium oxyacetylacetonate ($TiO(acac)_2$) precursor at varying final temperatures (T_{fin}). The microstructural parameters and phase composition of the TiO_2 NPs were determined via Rietveld refinement of X-ray diffraction (XRD) data. The PEC activity of spin-coated TiO_2/FTO photoanodes was evaluated via open-circuit potential (OCP) measurements, OCP decay, and linear sweep voltammetry (LSV) under chopped illumination. The results indicate that the anatase-rutile ratio and crystallite dimensions can be modulated by varying T_{fin} in the range of 500-700°C. An optimized mixed-phase TiO_2 comprising 71.7% anatase and 28.3% rutile, with the crystallite sizes D_{av} of 29.6 nm and 55.6 nm, respectively, is achieved at 650 °C enabling an efficient transition to free-electron transport and maximized photoactivity. These findings offer essential design principles for managing structural and phase transformations in TiO_2-based

photoanodes via the metal-organic decomposition route.

Keywords:

Photoelectrocatalysis, TiO_2, metal-organic decomposition, decomposition temperature, charge carrier dynamics

1. Introduction

The growing global energy crisis and environmental degradation have prompted extensive investigation into photoelectrocatalytic (PEC) water splitting as a promising approach for attaining carbon neutrality [1]. Since the pioneering development of titanium dioxide (TiO_2) photoanode, it has remained the benchmark semiconductor material for PEC and photocatalytic applications, owing to its remarkable chemical stability, resistance to photo corrosion, non-toxicity, affordability, and advantageous energy band alignment for water oxidation [2, 3]. However, the practical PEC efficiency of pristine TiO_2 remains restricted by its wide bandgap and rapid charge recombination, necessitating precise control over its crystal structure, morphology, and phase polymorph composition during synthesis [4]. The anatase-rutile composition and crystallite dimensions are known to significantly modulate the PEC performance of TiO_2 [5-7]. Specifically, mixed-phase materials can improve charge separation [6, 8, 9], while crystallite sizes govern specific surface area, charge-carrier dynamics and light absorption efficiency [10]. To control the structural and compositional parameters of TiO_2, the choice of an appropriate synthesis is crucial. Conventional synthesis of multi-phase TiO_2 commonly relies on wet-chemical methods such as hydrothermal treatment employing $TiCl_3$ as the titanium precursor [11, 12].

The metal-organic non-isothermal decomposition (MOD) pathway, using metal acetylacetonate ($M(acac)_n$) as precursor, represents a promising strategy for synthesizing advanced functional materials with tailored structural properties via control of processing parameters, including final decomposition temperature (T_{fin}) and heating rate [13-17]. Consequently, T_{fin} serves as a powerful parameter governing both crystallite growth kinetics and polymorphic phase transformations in TiO_2. However, a systematic understanding of the correlation linking the T_{fin} of the $TiO(acac)_2$ precursor to the structural evolution, phase ratios, and subsequent PEC

activity remains absent.

Herein, we investigate the photoelectrocatalysis on TiO_2 nanoparticles (NPs) derived from $TiO(acac)_2$ by evaluating the critical effect of the T_{fin} within a window of 500–700 °C. We elucidate the correlations linking crystalline phase evolution and crystallite sizes to the underlying interfacial charge-carrier dynamics and photocurrent densities. Our findings delineate an optimized processing window for the development of phase-engineered TiO_2 photoanodes derived from acetylacetonate complexes, offering essential design principles for the advancement of solar energy conversion devices.

2. Materials and Methods

2.1 Materials

Titanium (IV) oxyacetylacetonate ($TiO(acac)_2$), Sigma-Aldrich, 90% purity), isopropanol (C_3H_8O, LenReaktiv, Russia, 99.8% purity), sodium sulfate (Na_2SO_4, LenReaktiv, Russia, 99.5% purity), and sodium sulfite (Na_2SO_3, LenReaktiv, Russia, 98.0% purity) were used as received without further purification. Fluorine-doped tin oxide (FTO) coated glass substrates (1.1 mm thickness, sheet resistance of 10 Ω/sq) were purchased from Tihot Optics (China). Bidistilled water was used throughout all experimental procedures.

2.2 TiO_2 synthesis

To prepare TiO_2 NPs, a crystalline precursor of titanium (IV) oxyacetylacetonate ($TiO(acac)_2$) was placed into alumina crucibles and subjected to direct thermal calcination in a muffle furnace (Thermo Fisher Scientific, USA) under ambient air. The target final temperatures (T_{fin}) varied systematically: 500, 550, 600, 650, 700 °C, utilizing a constant heating rate of 3 °C/min. After cooling to room temperature, the resulting crystalline powders were collected and thoroughly ground in an agate mortar for further characterization.

2.3. Characterization

The crystalline phase composition and crystallite size metrics of the synthesized powders were determined by X-ray diffraction (XRD) using Cu-Kα radiation (λ = 0.15406 nm) on an ARL X'TRA X-ray diffractometer (Thermo Fisher Scientific Inc., USA). Measurements were performed in the 2θ range of 15° to 100° with a step size of 0.02°. These data were used for both qualitative phase analysis and quantitative

analysis of diffraction line broadening. To account for instrumental contributions, a diffraction pattern of a NIST LaB_6 standard reference material (SRM 660b) was acquired under identical experimental conditions. Quantitative phase fractions and average crystallite domain sizes (D_{av}) for both anatase and rutile polymorphs were extracted from full-profile XRD patterns across all thermal treatment steps. The refinement of XRD patterns by the Rietveld method was carried out using two linear combinations of spherical harmonics for the Laue class of each observed space group. The background was simulated with $2\theta^{-6}$ coefficients of a polynomial function.

2.4. PEC measurements

The PEC properties of TiO_2 NPs were examined in a three-electrode PEC cell featuring a quartz window (working area of 1 cm^2) with a 0.5 M Na_2SO_4 or 0.5 M Na_2SO_4+0.25 M Na_2SO_4 electrolyte, utilizing a PS-20 potentiostat (SmartStat, Russia). An Ag/AgCl (3.5 M) electrode was used as the reference electrode, while a Pt wire electrode was utilized as the counter electrode. The electrodes created with the synthesized materials served as the working electrodes. The synthesized powder (25 mg) underwent ultrasonic treatment in 500 µL of isopropanol for 1 hour to achieve a uniform dispersion. The resulting suspension was applied to a fluorine doped tin oxide (FTO) substrate using a spin coating technique (SpinNXG-P1AH, Apex Instruments, India) and subsequently subjected to thermal treatment at 200 °C for 30 minutes in a LF-7/11-G2 muffle furnace (LOIP, Russia) with a chamber capacity of 7 L to ensure optimal adhesion. A three-layered structure was prepared by applying 100 µL of the suspension per layer. Each layer was deposited using a two-step spin program: 1000 rpm for 10 s followed by 3000 rpm for 20 s. Before applying the coating to the FTO glass slides, they underwent a thorough cleaning process involving consecutive washes with detergent, acetone, and deionized water to remove all contaminants, followed by ultrasonication. The PEC activity was analyzed using illuminated open-circuit potential (OCP) and linear sweep voltammetry (LSV), along with photocurrent transient measurements. A solar simulator utilizing a 500 W Xenon lamp (AM 1.5 G) served as the light source. A schematic representation of the experimental process, illustrating the non-isothermal thermal decomposition, spin-coating photoanode deposition, and the three-electrode photoelectrochemical cell configuration, is presented in Figure 1.

3. Results and Discussion

3.1. XRD analysis

XRD patterns of TiO_2 NPs prepared via $TiO(acac)_2$ thermal decomposition with T_{fin} variation were presented in Figure 2. The microstructural parameters and phase fractions of the TiO_2 NPs derived from Rietveld refinement as a function of T_{fin} are presented in Table 1. The phase analysis indicates that at 500 °C, TiO_2 crystallizes as a mixture of anatase and brookite phases, with anatase content of 54% exhibiting ultra-small crystallite sizes D_{av} of 6.8 nm. At this temperature, the unit cell of the ultra-small anatase NPs undergoes considerable intrinsic lattice deformation. This is quantitatively demonstrated by the significantly reduced c/a ratio of 2.5039 at 500 °C compared to the standard bulk value of 2.5140. The change in lattice parameters can be a function of both the anion vacancy (hydroxyl) concentration in the nanocrystal and the intensity of the additional pressure imposed by the surface tension on the crystal, which are typical of very small crystallite boundaries [18, 19].

Simultaneously, the growth kinetics of the rutile phase demonstrate a significant dependence on temperature. Nucleation of the rutile polymorph is initially observed at 550 °C, exhibiting a minor phase fraction of 7.0% and an initial crystallite size of 19.3 nm. As T_{fin} increases from 550 °C to 700 °C, a swift phase transition occurs, leading to a significant rise in the rutile content from 7.0% to 89.5%. This suggests that the system has successfully surpassed the thermodynamic activation energy barrier associated with the anatase-to-rutile transition (ART). The ATR temperature varies in the range 400–1200 °C due to differences in particle size, aspect ratio, surface area, impurities, etc [20].

As the calcination temperature rises to 650 °C, the D_{av} increases continuously to 29.6 nm for anatase. Concurrently, the intrinsic lattice strain undergoes complete relaxation, as fundamentally indicated by the progressive increase of the c/a aspect ratio, which smoothly converges to 2.5144 at 650 °C. This stabilization represents the transition where the unit cell symmetry fully reaches its unconstrained bulk thermodynamic value. Above 650 °C, the ongoing thermal energy initiates a significant mass phase transformation into the denser rutile polymorph. At 700 °C, 89.5 % of rutile phase with D_{av} of 74.7 nm is formed.

3.2. OCP measurements

To establish a comprehensive understanding of the semiconductor band structure and the underlying charge transfer dynamics of TiO_2/FTO time-resolved open-circuit potential (OCP) transients were measured under controlled chopped illumination. Monitoring OCP variations provides direct insight into the band bending at the semiconductor/electrolyte interface, carrier mobility, and the density of structural defect traps [21, 22]. Figure 3a shows the OCP transients of TiO_2/FTO in dark and illuminated conditions in an aqueous Na_2SO_4 electrolyte. In the dark (light-off state), the immersion of the TiO_2 working electrode and the counter electrode into the electrolyte leads to the formation of a space-charge layer, which induces a characteristic internal electric field. Upon illumination (light-on state) with photon energy exceeding the semiconductor bandgap ($h\upsilon > E_g$), photogenerated electrons and holes are excited into the conduction and valence bands, respectively. Under open-circuit conditions, the built-in electric field within the space-charge region drives the photogenerated holes toward the semiconductor/electrolyte interface, while simultaneously sweeping the photoelectrons toward the FTO/semiconductor ohmic contact. This spatial separation of charge carriers establishes a non-zero photovoltage [23]. The negative (cathodic) shift in OCP upon illumination confirms the expected n-type conductivity of the synthesized TiO_2 NPs. The magnitude of this cathodic shift in OCP ($\Delta OCP = OCP_{light} - OCP_{dark}$) serves as a direct indicator of the charge separation efficiency. At 500 °C, the TiO_2 possesses a low anatase content 54% with tiny crystallites of 6.8 nm and substantial lattice deformation (c/a=2.5039). As the T_{fin} increases from 500 to 650°C, the steady-state potential under illumination shifts progressively toward more negative values (Figure 3a). The TiO_2 processed at 650 °C displays the sharpest, nearly vertical potential transients. This rapid response indicates exceptionally high carrier mobility which is well-supported by the crystallization behavior. Raising the temperature to 650 °C dramatically improves crystal quality: the anatase crystallite size grows to 29.6 nm, and the lattice parameters stabilize (c/a= 2.5144), minimizing internal stress and passivating defects that act as recombination centers. The maximum PEC response is achieved at 650 °C. At this specific condition, XRD reveals a mixed-phase composition consisting of 71.7 % anatase and 28.3 % rutile. However, at a synthesis temperature of 700 °C, the PEC performance degrades, and the curves shift upward. This attenuation is likely

induced by the thermal anatase-to-rutile phase transformation and excessive particle sintering, which reduces the effective electrochemically active surface area. Furthermore, the initial rate of the photopotential drop immediately after turning on the light (dOCP/dt) at t=60 s exhibits a significant dependence on temperature. Conversely, the more gradual slopes observed for the 500 °C and 700°C samples indicate obstructed charge transport dynamics caused by high defect density or detrimental grain boundary resistances.

The addition of Na_2SO_3 acting as a hole scavenger (Figure 3b) effectively suppresses surface recombination by rapidly scavenging the photogenerated holes, thereby increasing ΔOCP. This effect is attributed to the rapid consumption of photogenerated holes at the semiconductor/electrolyte interface, which effectively suppresses surface recombination and allows for a greater accumulation of electrons in the conduction band. In the presence of a hole scavenger, the illuminated OCP reached more cathodic values, closer to the theoretical E_{fb}. This suggests that the scavenger minimizes the influence of surface states and recombination centers, which otherwise prevent the bands from fully flattening under illumination. The observed insensitivity of Δ OCP to the presence of a hole scavenger in the 6.8 nm nanoparticles (Table 2) strongly implies that the charge carrier dynamics in these ultra-small crystallites are strictly trap-dominated rather than governed by interfacial transfer. In such a regime, the high surface-to-volume ratio and severe lattice distortion characteristic of sub-10 nm particles lead to a prominent density of structural defects, such as deep oxygen vacancies and dangling bonds. These defects introduce deep trap states located far within the bandgap. This rapid and rigid entrapment outcompetes the kinetics of interfacial charge transfer. Consequently, the photogenerated carriers become spatially isolated and chemically inaccessible, rendering the addition of external surface reactants or hole scavengers completely ineffective in modulating the overall photovoltage responses. Moreover, the cathodic shift of the OCP upon turning on the illumination for ultra-small particles was observed to be slower in the presence of a hole scavenger. The elimination of surface-bound holes by the scavenger may alter the occupancy of bulk trap states, forcing photogenerated electrons to navigate a more complex trap-filling path before reaching the steady-state Fermi level [24]. This slow response, combined with the fact that the final E_{fb} remains unchanged, reinforces the conclusion that the electronic structure of these ultra-small particles is governed by internal defect dynamics. The scavenger, while theoretically

aiding charge separation, appears to interfere with the rate at which the internal trap distribution reaches electronic equilibrium, likely due to a change in the surface potential or the reorganization of the Helmholtz layer. Thereby, if illumination is sufficiently intense and the carrier recombination rates in the semiconductor are not very large, the photovoltage can absolutely eliminate pre-existing band bending at the semiconductor/electrolyte interface [23]. The obtained ΔOCP significantly depends on the T_{fin}, which directly governs the structural and compositional parameters, along with the average crystallite size of the TiO_2 NPs (Table 2).

3.3. OCP decay measurements

To elucidate the electronic quality and charge carrier dynamics of the TiO_2 films prepared from the titanium acetylacetonate precursor, OCP decay curves after illumination turn off were comprehensively analyzed. The decay rate serves as an effective indicator of trap states in the photoanode material, as a swift decay suggests a reduced number of trap sites [25]. Figure 3c highlights the detailed view of the initial relaxation transient as the system returns to thermodynamic dark equilibrium in Na_2SO_4.

The average carrier lifetime was extracted from the tri-exponential potential decay profiles (1) using the amplitude-weighted lifetime formula (2) [26, 27]:

$$y(t) = A_0 + A_1 e^{-t/\tau_1} + A_2 e^{-t/\tau_2} + A_3 e^{-t/\tau_3} \quad (1)$$

$$\tau_{avg} = \frac{\sum |A_i| \cdot \tau_i}{\sum |A_i|} \quad (2)$$

where A_i parameters represent the pre-exponential amplitude factors corresponding to individual decay pathways, and τ_i denotes the respective time constants.

τ_{avg} represents the average time a generated charge carrier remains in the conduction or valence band before undergoing recombination, considering the amplitude of each decay pathway.

The total half-life (τ_{total}) was calculated using the Equation 3 [25] (4):

$$\tau_{total} = ln2 * \tau_m \quad (3)$$

where $\tau_m = \frac{\tau_1 \tau_2 \tau_3}{\tau_1 \tau_2 + \tau_2 \tau_3 + \tau_3 \tau_1}$ (4)

The calculated τ_{avg} and τ_{total} exhibit a distinct dependence on the T_{fin} (Figure 3d, e). The transient decay of the photopotential after turning off the illumination is

strictly governed by the detrapping rate of electrons from localized states within the bandgap [25]. Therefore, longer relaxation times directly signify a higher concentration of deep electron traps that artificially prolong the potential decay, whereas a shorter lifetime indicates an unobstructed, rapid recombination of free carriers due to a significantly reduced density of deep trap states [27-29]. Deconvolution of the OCPD fitting results yields distinct relaxation time constants, which are plotted as a function of the T_{fin} in Figure 3d, e.

A direct correlation with the XRD data perfectly rationalizes this kinetic behavior. At a relatively low calcination temperature of 500 °C, the TiO_2/FTO exhibits the longest carrier lifetime. Structurally, this sample is highly disordered, comprising 54% of crystalline anatase phase with an ultra-small crystallite size D_{av} = 6.8 nm, leaving nearly 46% of the material in a brookite phase. Upon light termination, photo-generated electrons become deeply trapped, severely delaying their recombination and generating a long decay tail.

As the T_{fin} increases from 500 to 650 °C, a systematic and dramatic reduction in τ_{total} down to its minimum value of 66.9 s is observed. This acceleration of the potential decay is driven by a profound structural refinement of the material. XRD analysis indicates that the thermal treatment withing this temperature window results in well-crystallized anatase and rutile phases. The anatase crystallites undergo substantial grain growth from 6.8 to 29.6 nm, while the rutile grains increase from 19.3 to 55.6 nm. Simultaneously, the lattice distortion of the anatase phase relaxes, which is clearly evidenced by the steady evolution of the c/a aspect ratio toward its ideal theoretical value (increasing from 2.5039 at 500 °C to 2.5144 at 650 °C). The sintering of small particles decreases the total area of detrimental grain boundaries, while the improvement of lattice tetragonality efficiently eliminates deep structural defects from the bulk. Remarkably, this point corresponds to a mixed-phase synergistic state consisting of 71.7% anatase and 28.3% rutile. This phase composition closely matches the internationally recognized benchmark for maximum photocatalytic and optoelectronic performance (e.g., Degussa P25). The formation of mixed-phase TiO_2 can play a pivotal role in suppressing electron-hole recombination leading to improved photocatalytic activity [30].

However, further increasing the temperature to 700 °C reverses the kinetic trend, causing τ to increase. This electronic degradation corresponds to a massive phase

transformation, where the anatase structure almost fully collapses (dropping to 10.5%), and the film becomes predominantly rutile (89.5%) with heavily sintered, large grains of D_{av}=74.4 nm.

The established correlation between the crystallite size and phase evolution and the drastic reduction of the photopotential decay time upon heating is in pristine agreement with the fundamental insights reported by Naniwa and co-workers [29]. In their study on charge carrier dynamics, it was explicitly demonstrated that the physical depth and overall density of electron trapping centers in anatase TiO_2 nanoparticles are strictly determined by the spatial confinement and geometric scale of the crystal lattice. Specifically, they found that ultrafine nanoparticles (ca. 6.3 nm) are heavily dominated by exceptionally deep midgap trap states located between 3.1 and 0.7 eV below the conduction band minimum, which physically capture almost the entire population of photoexcited electrons and severely retard their relaxation kinetics [29].

Thereby, the combination of large, well-crystallized anatase grains ~29.6 nm and the optimal amount of rutile secondary phase 28.3 % minimize the concentration of deep trapping states on the surface. Consequently, the rapid charge transport dynamics match perfectly with the maximum negative photopotential shift observed in Figures 2a and 2b, identifying 650°C as the optimal T_{fin} for maximizing the PEC efficiency of TiO_2/FTO photoanode.

3.4. PEC measurements

LSV under chopped illumination in the presence of a hole scavenger reflects the intrinsic photogeneration capacity and the charge-separation efficiency of the TiO_2 electrode [22]. As the T_{fin} increases from 500 °C to 650 °C, a progressive and substantial enhancement in the photocurrent density is observed. The TiO_2 annealed at 650 °C exhibits the highest PEC activity, reaching a maximum photocurrent density (Figure 4a) and demonstrating a significant cathodic shift of the E_{onset} (Figure 4b). This enhancement is attributed to the improved crystallinity, optimal size and phase composition, as well as passivation of defects, which collectively facilitates efficient charge separation under applied bias. However, a further increase in the annealing temperature to 700 °C leads to a noticeable degradation of the PEC performance, characterized by a decrease in photocurrent magnitude and a positive

shift of E_{onset}. This decline is likely driven by reduction in active surface area and lower activity of the rutile phase.

Thus, based on OCP and LSV measurements coupled with XRD analysis, it was established that the decomposition temperature of $TiO(acac)_2$) directly affects the lattice parameters, crystallite size, and phase composition (brookite, anatase, rutile) of the resulting TiO_2. These structural and phase characteristics, in turn, govern the trap density, photocurrent, photopotential (ΔOCP), and the onset oxidation potential. Consequently, the final decomposition temperature can be considered a dominant factor governing the PEC activity of TiO_2 fabricated via the non-isothermal decomposition of $TiO(acac)_2$.

4. Conclusions

This study successfully elucidated the structure- and phase-dependent PEC activity of TiO_2 NPs derived from $TiO(acac)_2$ by mapping the critical effect of the final non-isothermal decomposition temperature within a 500–700 °C window. Comprehensive Rietveld refinement of XRD data coupled with time-resolved photoelectrochemical analyses confirmed that T_{fin} acts as the primary governing factor that simultaneously dictates the phase evolution, crystallite dimensions, and subsequent charge-carrier dynamics of the synthesized TiO_2 NPs. Thermal treatment up to 650 °C facilitates lattice strain relaxation, resolves structural trapping-limited transport regimes, and eliminates deep localized defect states via the increase in crystallite size and formation of a synergistic anatase-rutile mixed-phase TiO_2. An optimized mixed-phase TiO_2 comprising 71.7% anatase and 28.3% rutile, with the crystallite sizes D_{av} of 29.6 nm and 55.6 nm, respectively, is achieved at 650 °C enabling maximized PEC activity, including a lower onset potential, improved photocurrent, and enhanced photopotential. Crucially, these findings advance the field of solar energy conversion by establishing material design principles for the scalable fabrication of optimized mixed-phase TiO_2 materials via the MOD route. Further development of this work, which is currently underway, focuses on evaluating the heating rate effects and tailoring the photoanode fabrication parameters to maximize PEC efficiency.

Acknowledgment

This work was supported by the Russian Science Foundation, project № 25-19-00280.

CRediT Author Statement

Anna Ulyankina: Writing Draft Preparation, Visualization; *Daria Bondareva*: Methodology, Investigation; *Tatyana Belichenko*: Methodology, Formal Analysis, Data Curation, Investigation; *Yash Kataria*: Methodology, Formal Analysis, Data Curation; *Aydar Rakhmatullin:* Methodology, Formal Analysis; *Igor Leontyev:* Methodology, Formal Analysis; Investigation: *Nina Smirnova*: Writing, Review and Editing, Resources. All the authors have read and agreed to the published version of the manuscript.

References

[1] Shevchenko, Y., Bakranov, N., Serikkanov, A., Bakranova, D. (2026). Photoelectrochemical pathways to green hydrogen. analysis, overview, and foresight. *Renewable and Sustainable Energy Reviews*, 231, 116753. DOI:10.1016/j.rser.2026.116753

[2] Feng, T., Yam, F.K. (2025). A review of TiO_2 nanostructured materials for hydrogen generation through photocatalytic and photoelectrochemical water splitting. *Physica B: Condensed Matter*, 714, 417466. DOI:10.1016/j.physb.2025.417466

[3] Dao Duy, N., Vu Minh, T., Huynh Trung, H., Thu Vu, H.T. (2026). Effect of Calcination Temperature on Structural Properties and Photocatalytic Activity of TiO_2/Vermiculite Composite for Methylene Blue Degradation. *Bulletin of Chemical Reaction Engineering & Catalysis*, 21 (3), 600-610. DOI:10.9767/bcrec.20736

[4] Ye, Y., Shen, J., Wang, A., Yang, R., Liang, S. (2025). Sophorolipid-directed microemulsion synthesis of TiO_2 nanoparticles with controllable size and high photocatalytic efficiency. *Colloids and Surfaces A: Physicochemical and Engineering Aspects*, 726, 137822. DOI:10.1016/j.colsurfa.2025.137822

[5] Ningthoukhongjam, P., K, N.S., Kumar P, M., Bhagavathiachari, M., Nair, R.G. (2022). Effect of anatase-rutile phase ratio of titania photoanode on photoelectrochemical performance and photoconversion efficiency. *Optical Materials*, 127, 112269. DOI:10.1016/j.optmat.2022.112269

[6] Ulyankina, A., Kravchenko, D., Belichenko, T., Gorshenkov, M., Leontyev, I., Faddeev, N., Yatsenko, A., Ponomarev, D., Rakhmatullin, A., Zhigunov, D., Smirnova, N. (2026). Electrochemical Phase Engineering of Anatase/Rutile/Brookite TiO2 Nanopowders via Pulsed Alternating Current for Photocatalytic Water Remediation. *Journal of Electrochemical Science and Technology*, DOI:10.33961/jecst.2026.00059

[7] Chen, W.-T., Chan, A., Jovic, V., Sun-Waterhouse, D., Murai, K.-i., Idriss, H., Waterhouse, G.I.N. (2015). Effect of the TiO_2 Crystallite Size, TiO_2 Polymorph and Test Conditions on the Photo-Oxidation Rate of Aqueous Methylene Blue. *Topics in Catalysis*, 58, 85-102. DOI:10.1007/s11244-014-0348-7

[8] Stepanova, A., Tite, T., Ivanenko, I., Enculescu, M., Radu, C., Culita, D.C., Rostas, A.M., Galca, A.C. (2023). TiO_2 Phase Ratio's Contribution to the Photocatalytic Activity. *ACS Omega*, 8, 41664-41673. DOI:10.1021/acsomega.3c05890

[9] Eddy, D.R., Permana, M.D., Sakti, L.K., Sheha, G.A.N., Solihudin, Hidayat, S., Takei, T., Kumada, N., Rahayu, I. (2023). Heterophase Polymorph of TiO_2 (Anatase, Rutile, Brookite, TiO_2 (B)) for Efficient Photocatalyst: Fabrication and Activity. *Nanomaterials*, 13 (4), 704. DOI: 10.3390/nano13040704

[10] Kočí, K., Obalová, L., Matějová, L., Plachá, D., Lacný, Z., Jirkovský, J., Šolcová, O. (2009). Effect of TiO2 particle size on the photocatalytic reduction of CO2. *Applied Catalysis B: Environmental*, 89, 494-502. DOI:10.1016/j.apcatb.2009.01.010

[11] Li, H., Shen, X., Liu, Y., Wang, L., Lei, J., Zhang, J. (2015). Facile phase control for hydrothermal synthesis of anatase-rutile TiO2 with enhanced photocatalytic activity. *Journal of Alloys and Compounds*, 646, 380-386. DOI:10.1016/j.jallcom.2015.05.145

[12] Stepanova, A., Tite, T., Ivanenko, I., Enculescu, M., Radu, C., Culita, D.C., Rostas, A.M., Galca, A.C. (2023). TiO2 Phase Ratio's Contribution to the Photocatalytic Activity. *ACS Omega*, 8, 41664-41673. DOI:10.1021/acsomega.3c05890

[13] Ivanova, A.V., Ivanova, E.V., Nikitin, A.A., Cherepanov, V.M., Abakumov, M.A. (2024). Thermal decomposition of acetylacetonates for highly reproducible synthesis of M-ferrite (Mn, Co and Zn) nanoparticles with tunable magnetic

properties. *Journal of Alloys and Compounds*, 976, 172737. DOI:10.1016/j.jallcom.2023.172737

[14] Donaire Pereyra, F.Y., Marin-Ramirez, O. (2025). On the properties of CuO/ZnO heterostructures obtained via thermal decomposition of metal acetates: Role of precursor strategy. *Next Materials*, 9, 100957. DOI:10.1016/j.nxmate.2025.100957

[15] Kuriganova, A., Smirnova, N., Yatsenko, A., Gorshenkov, M., Leontyev, N., Allix, M., Rakhmatullin, A., Leontyev, I. (2025). Basic features of Pt/C catalysts synthesised via the non-isothermal decomposition of platinum acetylacetonate. *Nanoscale*, 17, 18787-18795. DOI:10.1039/D5NR01487E

[16] Xiong, L., Xu, Y., Lei, P., Tao, T., Xiao, X. (2014). Synthesis and characterization of TiO_2/C by a simple thermal decomposition method. *Solid State Ionics*, 268, 265-267. DOI:10.1016/j.ssi.2014.08.009

[17] Kulbakov, A.A., Allix, M., Rakhmatullin, A., Mikheykin, A.S., Popov, Y.V., Smirnova, N.V., Maslova, O., Leontyev, I.N. (2018). In Situ Investigation of Non-Isothermal Decomposition of Pt Acetylacetonate as One-Step Size-Controlled Synthesis of Pt Nanoparticles. *Physica Status Solidi (A)*, 215, 1800488. DOI:10.1002/pssa.201800488

[18] Huang, Z., Thomson, P., Di, S. (2007). Lattice contractions of a nanoparticle due to the surface tension: A model of elasticity. *Journal of Physics and Chemistry of Solids*, 68, 530-535. DOI:10.1016/j.jpcs.2007.01.016

[19] Chen, L., Fleming, P., Morris, V., Holmes, J.D., Morris, M.A. (2010). Size-Related Lattice Parameter Changes and Surface Defects in Ceria Nanocrystals. *The Journal of Physical Chemistry C*, 114, 12909-12919. 10.1021/jp1031465

[20] Hanaor, D.A.H., Sorrell, C.C. (2011). Review of the anatase to rutile phase transformation. *Journal of Materials Science*, 46, 855-874. DOI:10.1007/s10853-010-5113-0

[21] Hankin, A., Bedoya-Lora, F.E., Alexander, J.C., Regoutz, A., Kelsall, G.H. (2019). Flat band potential determination: avoiding the pitfalls. *Journal of Materials Chemistry A*, 7, 26162-26176. DOI:10.1039/C9TA09569A

[22] Koshevoy, E., Gribov, E., Polskikh, D., Lyulyukin, M., Solovyeva, M., Cherepanova, S., Kozlov, D., Selishchev, D. (2023). Photoelectrochemical Methods for the Determination of the Flat-Band Potential in Semiconducting

Photocatalysts: A Comparison Study. *Langmuir*, 39, 13466-13480. DOI:10.1021/acs.langmuir.3c01158

[23] Zare, M., Solaymani, S., Shafiekhani, A., Kulesza, S., Ţălu, Ş., Bramowicz, M. (2018). Evolution of rough-surface geometry and crystalline structures of aligned TiO_2 nanotubes for photoelectrochemical water splitting. *Scientific Reports*, 8, 10870. DOI:10.1038/s41598-018-29247-3

[24] Ulyankina, A., Tsarenko, A., Molodtsova, T., Yatsenko, A., Gorshenkov, M., Kaichev, V., Kuriganova, A., Smirnova, N. (2023). Tungsten oxide nanopowders: pulse alternating current electrosynthesis, structure optimization and performance in a flow photocatalytic fuel cell. *Journal of Materials Science*, 58, 11187-11197. DOI:10.1007/s10853-023-08697-9

[25] Mukherjee, B., Wilson, W., Subramanian, V. (2013). TiO_2 nanotube (T_NT) surface treatment revisited: Implications of ZnO, $TiCl_4$, and H_2O_2 treatment on the photoelectrochemical properties of T_NT and T_NT–CdSe. *Nanoscale*, 5, 269-274. DOI:10.1039/c2nr31660a

[26] Pu, Y.-C., Wang, G., Chang, K.-D., Ling, Y., Lin, Y.-K., Fitzmorris, B.C., Liu, C.-M., Lu, X., Tong, Y., Zhang, J.Z., Hsu, Y.-J., Li, Y. (2013). Au Nanostructure-Decorated TiO2 Nanowires Exhibiting Photoactivity Across Entire UV-visible Region for Photoelectrochemical Water Splitting. *Nano Letters*, 13, 3817-3823. DOI:10.1021/nl4018385

[27] Ruan, Q., Bayazit, M.K., Kiran, V., Xie, J., Wang, Y., Tang, J. (2019). Key factors affecting photoelectrochemical performance of g-C3N4 polymer films. *Chemical Communications*, 55, 7191-7194. DOI:10.1039/C9CC03084K

[28] Katayama, K., Chugenji, T., Kawaguchi, K. (2021). Charge Carrier Trapping during Diffusion Generally Observed for Particulate Photocatalytic Films. *Energies*, 14, 7011. DOI:10.3390/en14217011

[29] Naniwa, S., Kato, K., Yamamoto, A., Yoshida, H., Yamakata, A. (2023). Particle Size Dependent Trap States of Photoexcited Carriers in Anatase TiO_2 Nanoparticles. *The Journal of Physical Chemistry C*, 127, 4295-4302. DOI:10.1021/acs.jpcc.2c08125

[30] Wang, W.-K., Chen, J.-J., Zhang, X., Huang, Y.-X., Li, W.-W., Yu, H.-Q. (2016). Self-induced synthesis of phase-junction TiO_2 with a tailored rutile to anatase

ratio below phase transition temperature. *Scientific Reports*, 6, 20491. DOI: 10.1038/srep20491

FIGURE CAPTIONS

Figure 1. Schematic representation of the experimental process

Figure 2. XRD patterns of TiO_2 NPs prepared via non-isothermal decomposition of $TiO(acac)_2$ at various T_{fin}

Figure 3. PEC properties and charge carrier relaxation kinetics of the TiO_2 prepared at different T_{fin}: Transient OCP profiles recorded under chopped illumination (a) without and (b) with hole scavenger; (c) Normalized OCP decay curves plotted as a function of time after light termination; (d) Decomposition temperature-dependence of the τ_{avg} (d) and τ_{total} (e) extracted from multi-exponential fitting of the OCP decay curves

Figure 4. (a) LSV curves of the TiO_2 photoanodes under chopped light-dark illumination as a function of T_{fin}; (b) E_{onset} determination from LSV curves

TABLE CAPTIONS

Table 1. Phase content, lattice parameter c/a and D_{av} of TiO_2 NPs at different T_{fin}

Table 2. PEC parameters of TiO_2 depending on T_{fin}

Table 1. Phase content, lattice parameter c/a and D_{av} of TiO_2 NPs at different T_{fin}

Parameter	T_{fin}, °C				
	500	550	600	650	700
Anatase content, %	54*	93.0	87.7	71.7	10.5
D_{av} (Anatase), nm	6.8	12.1	17.5	29.6	43.4
c/a (Anatase)	2.5039	2.5091	2.5128	2.5144	2.5148
Rutile content, %	-	7.0	12.3	28.3	89.5
D_{av} (Rutile), nm	-	19.3	36.3	55.6	74.4
c/a (Rutile)	-	0.6437	0.6439	0.6443	0.6443

Table 2. PEC parameters of TiO_2 depending on T_{fin}

Temperature, °C	LSV onset potential, V vs RHE	ΔOCP, V without hole scavenger	ΔOCP, V with hole scavenger
500	0.42	0.20	0.20
550	0.22	0.23	0.51
600	0.10	0.25	0.65
650	0.00	0.37	0.71
700	0.25	0.26	0.52

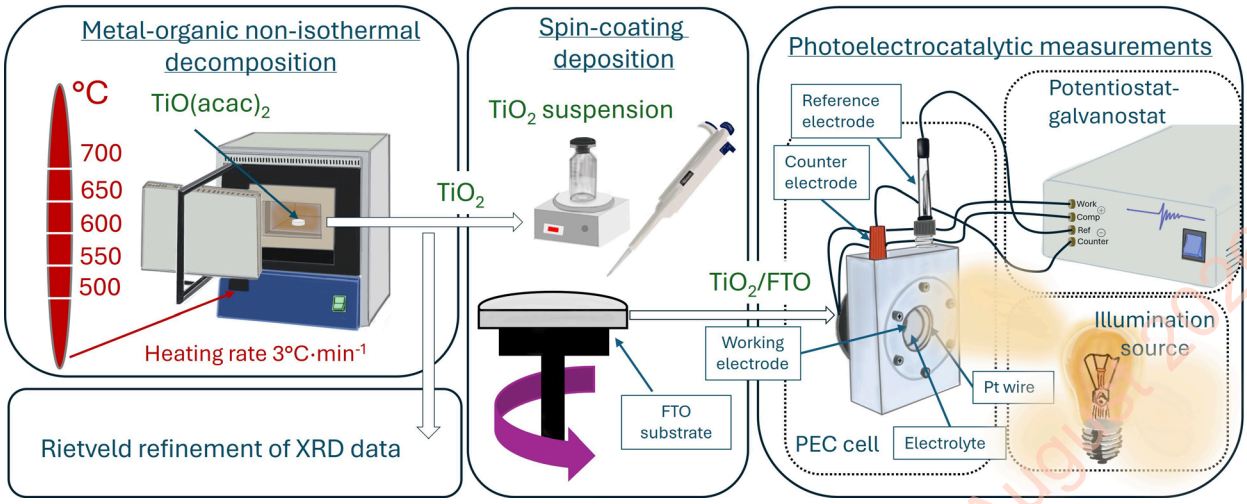

Figure 1. Schematic representation of the experimental process

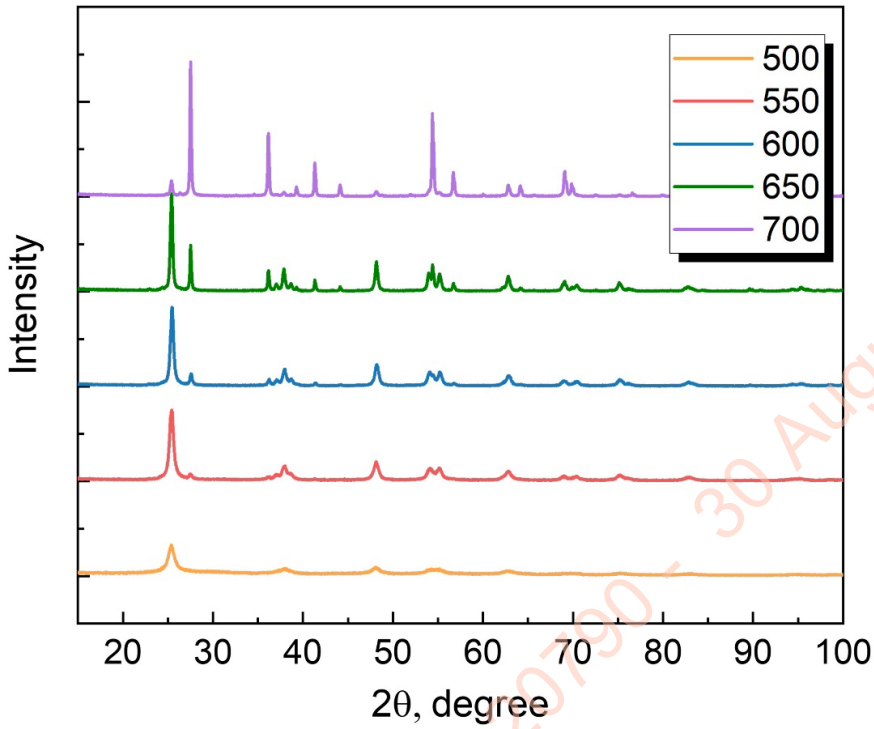

Figure 2. XRD patterns of TiO_2 NPs prepared via non-isothermal decomposition of $TiO(acac)_2$ at various T_{fin}

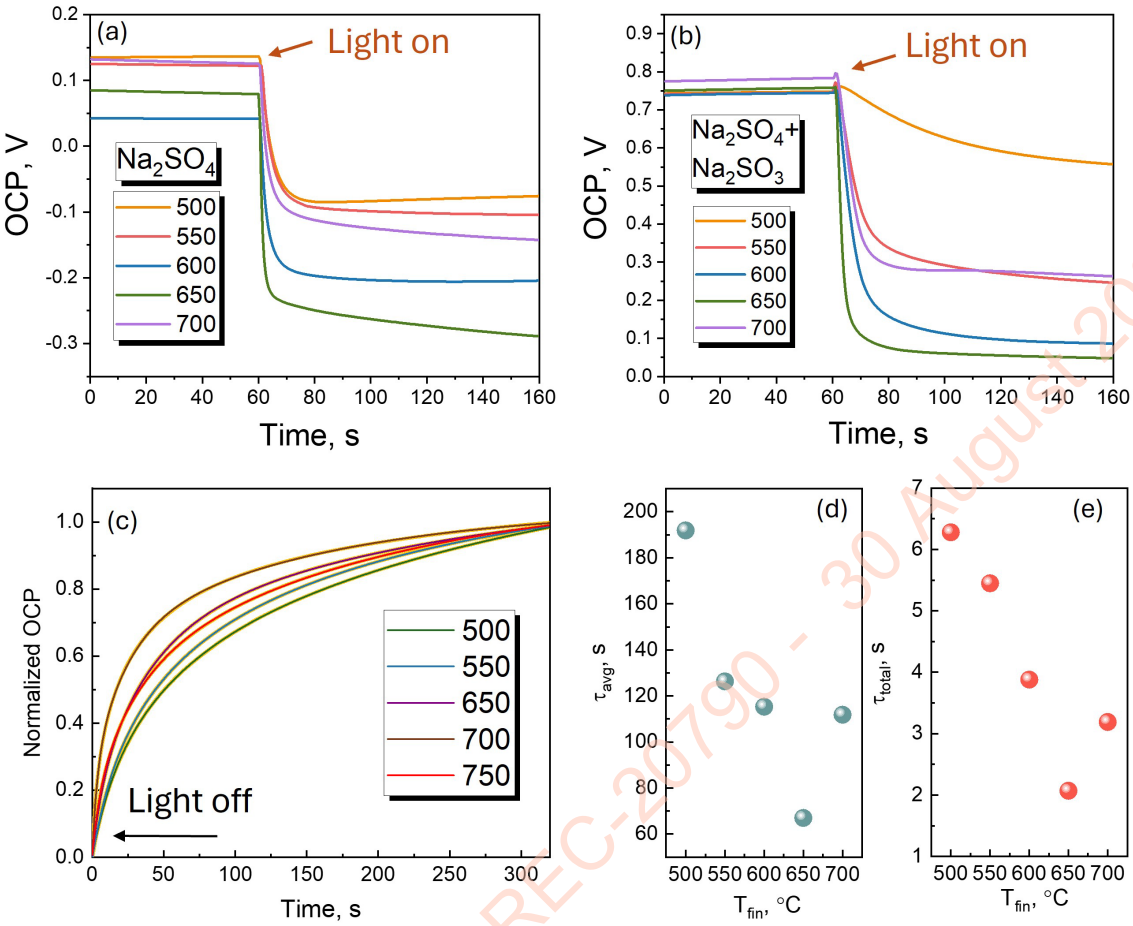

Figure 3. PEC properties and charge carrier relaxation kinetics of the TiO_2 prepared at different T_{fin}: Transient OCP profiles recorded under chopped illumination (a) without and (b) with hole scavenger; (c) Normalized OCP decay curves plotted as a function of time after light termination; (d) Decomposition temperature-dependence of the τ_{avg} (d) and τ_{total} (e) extracted from multi-exponential fitting of the OCP decay curves

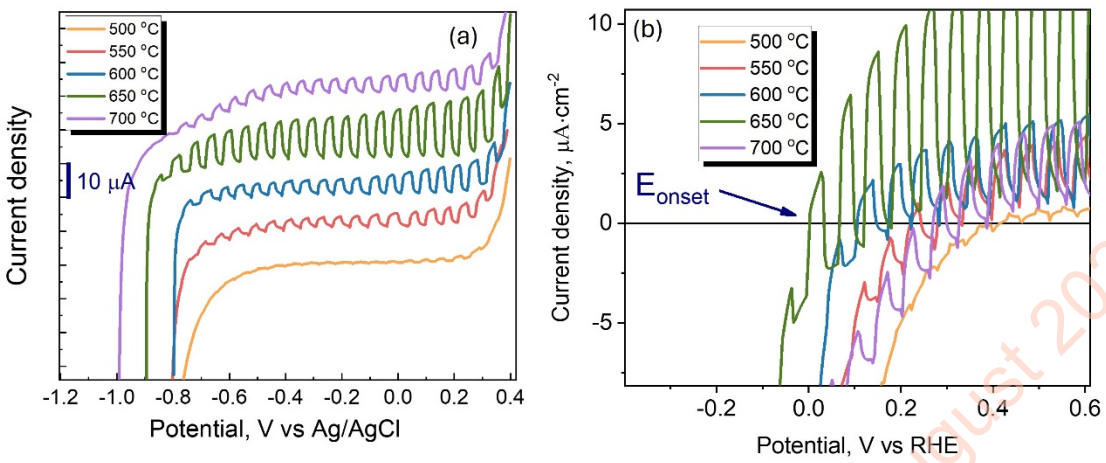

Figure 4. (a) LSV curves of the TiO_2 photoanodes under chopped light-dark illumination as a function of T_{fin}; (b) E_{onset} determination from LSV curves